Carbon *K*-shell photoionization of fixed-in-space C_2H_4

T. Osipov,[1] M. Stener,[2,3] A. Belkacem,[1] M. Schöffler,[1] Th. Weber,[1] L. Schmidt,[4] A. Landers,[5] M. H. Prior,[1] R. Dörner,[4] and C. L. Cocke[6,*]

[1]*Lawrence Berkeley National Laboratory, Chemical Sciences, Berkeley, California 94720, USA*

[2]*Dipartimento di Scienze Chimiche, Università di Trieste, Via L. Giorgieri 1, I-34127 Trieste, Italy*

[3]*Consorzio Interuniversitario Nazionale per la Scienza e Tecnologia dei Materiali (INSTM), Unita' di Trieste, Via L. Giorgieri 1, I-34127 Trieste, Italy*

[4]*Institut fur Kernphysik, University Frankfurt, Max von Laue Str 1, D-60438 Frankfurt, Germany*

[5]*Department of Physics, Auburn University, Alabama 36849, USA*

[6]*Department of Physics, Kansas State University, Manhattan, Kansas 66506, USA*

(Received 21 December 2009; published 31 March 2010)

Measurements of the photoelectron angular distributions in the body-fixed frame (MFPAD) have been carried out for 290- to 320-eV photons (just above the carbon *K*-shell ionization threshold) on C_2H_4 using an approach based on cold-target recoil-ion momentum spectroscopy (COLTRIMS). The results are compared with a theoretical calculation and excellent agreement is found. A direct verification of the "*f*-wave shape resonance" is accomplished by obtaining the complex amplitude of the $l = 3$ partial wave, which shows a peak in its absolute value and a relative phase change of π as the energy is scanned across the resonance.

DOI: 10.1103/PhysRevA.81.033429 PACS number(s): 33.80.Eh, 33.90.+h

I. INTRODUCTION

When conventional photoionization experiments are performed in the gas phase, they typically measure the cross section and the angular distribution of the emitted photoelectrons from a sample of molecules randomly oriented with respect to the laboratory frame. It is intrinsic for such an experiment that much information is lost due to the rotational average of all possible molecular orientations. For randomly aligned or oriented molecular targets it can be shown that (for each ionic state and for nonchiral molecules) only two parameters are sufficient to describe completely the photoelectron distribution; namely the cross section and the asymmetry parameter.

In recent years it has become possible to carry out measurements of the photoelectron [and other fragment(s)] angular distributions in the body-fixed frame of the molecule by using coincidence techniques. The basic idea is to reconstruct the molecular orientation with respect to the laboratory frame from the direction of the final ion fragments (see [1] for the pioneering experiment). The technique is based on the assumption that the molecular-fragmentation time is much shorter than the rotational period of the molecule (axial-recoil approximation, see [2–4] for a discussion of its limits of validity). Moreover, the photoionization must be followed by a fast fragmentation into ionic products. In the present case, we explore the photoionization of a core electron (*K* shell) in the molecule. When the core electron is ionized, the core hole undergoes a fast decay by emission of a secondary Auger electron and the resulting dication promptly breaks up though Coulomb explosion.

The most efficient approach for these types of multiple coincidence experiments today is the technique of cold-target recoil-ion momentum spectroscopy (COLTRIMS) [5,6]. The result of a COLTRIMS experiment consists of the complete description of the photoelectron angular distribution from a fixed-in-space (aligned) molecule, which can be characterized entirely by a series of parameters C_{LM} [see expression (4) below], where the integer L ranges from 0 up to (in principle) infinity, while the integer M is subject to the condition $-L \leqslant M \leqslant L$. Such parameters contain the maximum information which can be extracted by a photoionization experiment. This information provides important insights into the structure of the target molecule and its product ions, as well as into specific phenomena such as shape resonances which are directly affected by this structure.

II. EXPERIMENTAL SETUP AND DATA ACQUISITION

We examined ethylene (C_2H_4) photoionization for photon energies just above (2–30 eV) the *K*-shell ionization threshold. When a *K* electron is removed, this is followed by an Auger decay which in turn results in the Coulomb explosion of the molecular dication into two fragment ions. We detect the photoelectron and the two fragment ions in coincidence using a COLTRIMS setup (see [5–7]). The experimental system is a parallel-plate time-of-flight (TOF) spectrometer consisting of three different electric field regions separated by high (~80%) transmittance grids. RoentDek position-sensitive delay line detectors (see [8,9]) with 0.5-ns time resolution and 0.25-mm position resolution (defined by the electronic modules used for the data collection) were placed at both ends of the spectrometer. One detector served to collect all positively charged recoil ions and the other to collect the photoelectrons. For each ion and electron, the full momentum vector was calculated from the flight time and position with which that particle struck the detector. Data used for the analysis presented in this article were collected over several run-time periods during which a slightly different geometry of the spectrometer acceleration regions was used. Typically, the middle region would have a low field (~10 V/cm) and the other two would serve as field-free drift regions for the negative

*cocke@phys.ksu.edu

and positive sides of the spectrometer. This arrangement, together with the position information, allowed for a sub-eV energy resolution in both photoelectron and positive ion detection. To make sure that the electron momentum along the TOF direction had sufficient resolution, the corresponding side of the spectrometer usually had the time-focusing fields arrangement (see [10]) and was longer than the positive-recoil side. To confine the photoelectron transverse-flight spread to not exceed the spectrometer transverse size, a magnetic field of typically 10 G was maintained in the direction collinear to the spectrometer axis (TOF direction). This field was produced by the two large-diameter coils placed outside the chamber in the Helmholtz geometry. The magnetic field made electrons spiral toward the detector while having a negligible effect on the trajectories of the heavy positive ion (see [11]). The proper combination of the electric field of the spectrometer, flight distance, and the magnetic field strength insures that the electron momentum reconstruction can be done properly for the whole 4π solid angle. The vertical supersonic gas jet was used to deliver the target molecules to the interaction region. The lateral size of the jet at the interaction region was less than 2 mm and its density was near 10^{10}–10^{11} particles per cm^3 (local equivalent pressure of 10^{-7}–10^{-6} Torr, the temperature of the expanding gas being around 100 K) while the chamber vacuum was kept near 10^{-8} Torr. The x-ray photon beam propagation direction was horizontal and perpendicular to both the spectrometer axis and the gas jet direction.

The source of the photons was the Advanced Light Source at the Berkeley National Laboratory. The range of photon energies used for the reaction was 290–320 eV. Most of the experiments were conducted at beamlines 4.0.2 and 9.2.3 during the semiannual two-bunch periods essential for the TOF measurements. During the operation at beamline 4.0.2 the polarization of the light could be changed continuously from circular to linear oriented at any direction in the plane defined by the spectrometer axis and jet direction. At beamline 9.2.3, the polarization was fixed in the direction of the spectrometer axis and was not changeable. Detection of each photoelectron and two corresponding molecular-ion recoils produced after the *K*-shell photoionization was done in coincidence. The data were collected in the event-by-event mode. This allowed us to perform the fully differential reaction cross-section analysis.

III. DATA ANALYSIS

The analysis of the experimental data obtained for the reactions involving the molecular breakup is usually done by first looking at the photoion-photoion-coincidence (PIPICO) spectrum, which consists of a two-dimensional plot of the TOF of the second recoil versus the TOF of the first recoil. Such a plot (see Fig. 1) immediately reveals numerous possible and accessible breakup channels of the system at hand. In the particular case of C_2H_4, the main channel of interest is the so-called symmetric channel ($C_2H_4 \rightarrow CH_2^+ + C_2^+$)—here the initial direction of the C–C bond is preserved in the direction of the final recoil momenta. Besides the sharp hyperbolic-like curve representing this symmetric channel, the deprotonation channel ($C_2H_4 \rightarrow C_2H_3^+ + p$) and multiple three- and four-body breakup channels are readily identified. After setting

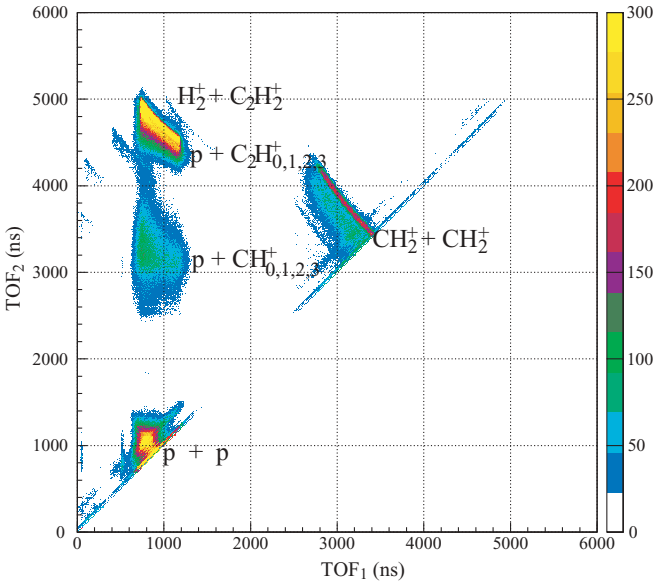

FIG. 1. (Color) C_2H_4 photoion-photoion coincidence (PIPICO). The hyperbolic segment, extending from $\text{tof}_1 = \text{tof}_2 \simeq 3400$ ns and labeled $CH_2^+ + CH_2^+$, is the main subject of this article.

the gate around the symmetric breakup in this manner a full three-dimensional momentum vector reconstruction was performed for all of the detected particles for each event. The longitudinal component of the momentum (the component along the spectrometer axis direction) was calculated from the TOF of the particle, its mass, its charge, and the known values of the extraction field and the spectrometer dimensions. The components of the momentum in the plane of the detector for the recoils were simply obtained by multiplying the corresponding velocity by the mass of the fragment. The velocity is given by the ratio of the displacement from the center of the detector to the fragment's TOF. The electron-side transverse-momentum calculation involves the use of a rotation matrix to reverse the effect of the spiraling due to the magnetic field. The exact detailed formulas for the above calculation are given elsewhere (e.g., see [7]).

The momentum vector of the CH_2^+ recoils was used to determine the initial molecular frame (C–C bond direction), The observed sharp features in the measured photoelectron angular distributions (see Fig. 2) indicate that the axial-recoil approximation works very well in this case. The absolute value of the recoil momentum vectors is trivially converted into the kinetic energy release (KER) of the molecular explosion (see Fig. 2). In case of the hydrocarbons and ethylene, in particular, this spectrum reveals a single KER peak, unlike the rich structure which was seen earlier for the CO and N_2 [4] molecular breakups produced in similar *K*-shell photoionization reactions. Apparently, the symmetric breakup of the dication of ethylene populated in this way is produced through only a single intermediate channel with a well-defined KER.

A similar analysis of the photoelectron energy shows the presence of satellite electrons in addition to the ones whose energy is consistent with the simple difference between the photon energy and the *K*-shell ionization potential. These satellite electrons are seen especially clearly on the two-dimensional

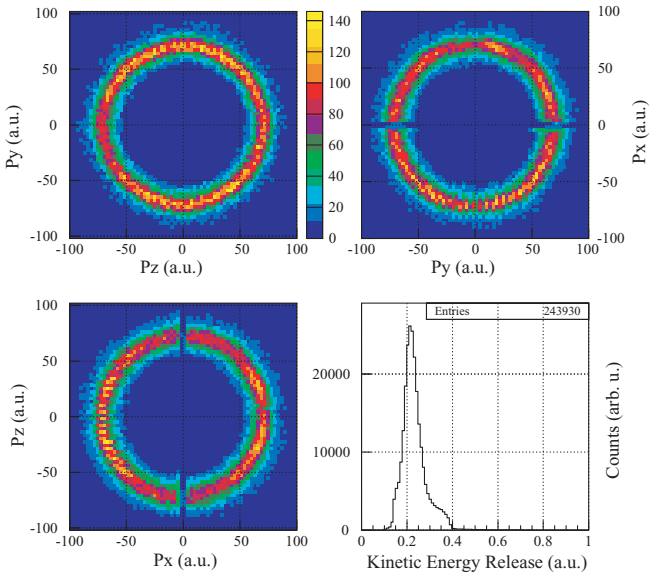

FIG. 2. (Color) $CH_2^+ + CH_2^+$ breakup-channel recoil-momentum slices and KER spectrum.

plot of the photoelectron energy versus the photon energy in Fig. 3. Thus, we avoid any satellite contamination of the resulting total photoionization cross section by gating on the main diagonal line in Fig. 3. This contamination was discussed by Kempgens *et al.* [12] in connection with attempts to identify or challenge the existence of f-wave resonance structure in the photoionization of hydrocarbons in this photon region. Except in Fig. 5, all further plots in this paper represent main-line data only, excluding satellites.

Calculation of the momentum vectors for both recoils and for the photoelectron on an event-by-event basis allows for the measurement of the angle between these vectors. Since the direction of the relative momentum of the two

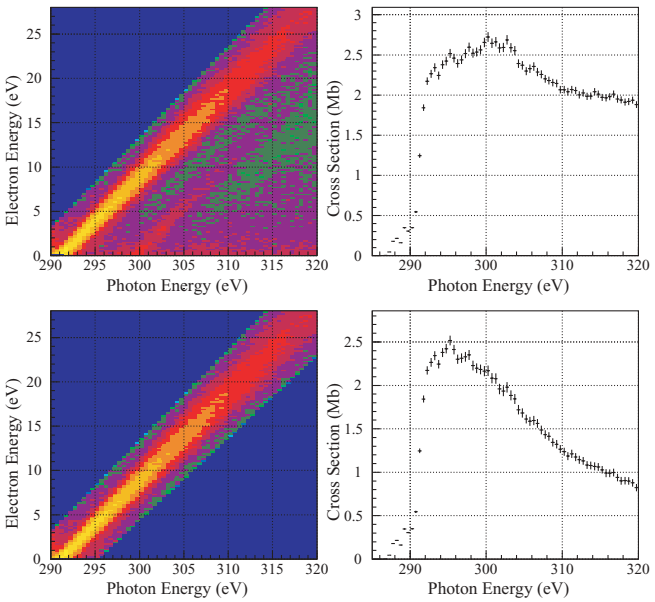

FIG. 3. (Color) Electron energy as a function of the photon energy and the corresponding cross sections for the carbon 1s main line plus satellites (top) and the main line only (bottom).

recoil ions denotes the molecular orientation, the direction of the photoelectron with respect to this orientation gives a unique angular distribution in the molecular body-fixed frame. Note that experimental data and analysis just presented allow only for determination of the C–C bond orientation. The plane of the molecule is undefined (implicitly averaged over). Thus all references made here to the experimental photoelectron angular distributions in the molecular body-fixed frame assume this specific definition of it. Figure 4 is the example of the polar-plot representation of this measured angular distribution data for 306-eV linearly polarized photons with a 0°–90° angular range between the C–C bond orientation and the polarization direction. Due to the symmetry of the molecule only half of each polar plot (one quarter for 0° and 90° frames) represents the unique data, the rest is just appropriately rotated or reflected duplicates. The solid curve on top of the experimental error bars here is the best fit done with the following fitting formula:

$$f(\hat{k},\theta)|_{A_l,B_l} \propto \left|\sum_{l=0,2} A_l Y_l^0(\hat{k})\cos\theta + \sum_{l=0,2}\frac{B_l}{\sqrt{2}}\left[Y_l^{-1}(\hat{k}) - Y_l^1(\hat{k})\right]\sin\theta\right|^2 + \left|\sum_{l=1,3} A_l Y_l^0(\hat{k})\cos\theta + \sum_{l=1,3}\frac{B_l}{\sqrt{2}}\left[Y_l^{-1}(\hat{k}) - Y_l^1(\hat{k})\right]\sin\theta\right|^2, \quad (1)$$

where θ is the angle between the polarization direction and the molecular axis, $\hat{k}$ is the direction of the photoelectron in the molecular frame, A_l and B_l are complex-valued fitting parameters independent of θ and $\hat{k}$. The discussion of this fitting function form is given in Sec. V below (see also [7]).

IV. THEORETICAL METHOD

To compare with the results of experimental measurements of the photoelectron angular distributions in the body-fixed frame (MFPADs), we calculated theoretical molecular MFPADs. We employed the Kohn-Sham (KS) B-spline linear combination of atomic orbitals (LCAO) formalism for the calculation of the continuum. The formalism is fully described in [13], so here we sketch only the essential points.

A ground state KS calculation of the electronic structure is first performed, employing the second Amsterdam density functional (ADF) program [14] with a double-zeta polarized (DZP) basis set of Slater-type orbitals and the van Leeuwen and Baerends [15] (LB94) [15] exchange-correlation potential. The LB94 is chosen because of its correct asymptotic Coulomb behavior, which has proven important for an accurate description of the photoionization dynamics at the KS level. The electron density obtained with the ADF program is then employed to represent the KS Hamiltonian matrix employing the LCAO B-spline basis set. Occupied orbitals are obtained as bound eigenvectors: $H_{KS}\varphi_i = \varepsilon_i\varphi_i$, $i = 1, \ldots, n$. Continuum photoelectron orbitals are extracted as eigenvectors with minimum modulus eigenvalue of the energy-dependent matrix $\mathbf{A}^+\mathbf{A}$:

$$\mathbf{A}^+\mathbf{A}(E)c = ac, \quad \mathbf{A}(E) = \mathbf{H} - E\mathbf{S}. \quad (2)$$

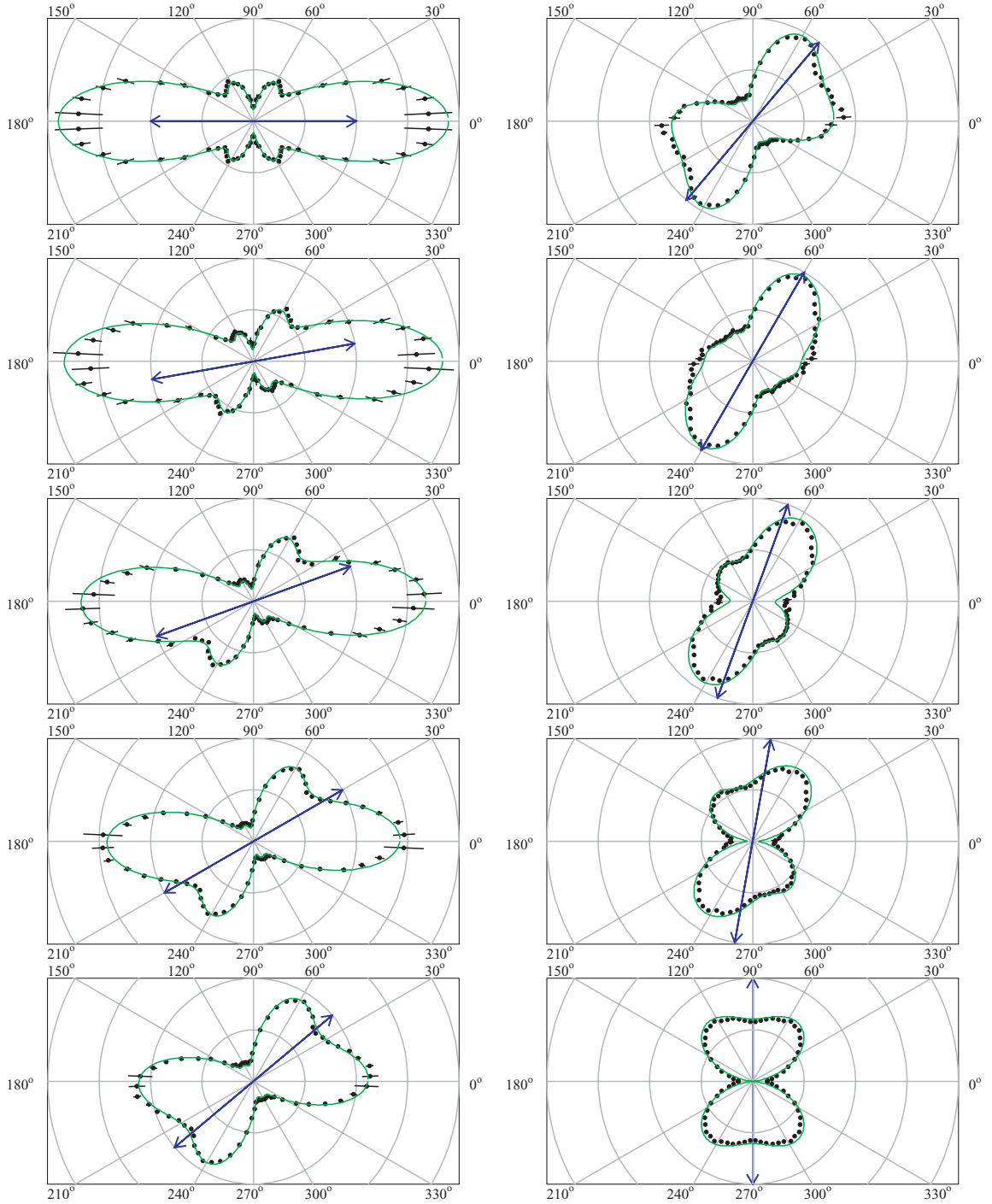

FIG. 4. (Color) Electron angular distribution at 306-eV photon energy. The arrow shows the polarization direction. Molecular orientation is always along the x axis. All frames are plotted with the same scale by default.

In equation (2), **H** and **S** are the Hamiltonian and overlap matrices respectively, E is the photoelectron kinetic energy, c are the eigenvectors and a are the minimum modulus eigenvalues. The quantities c, which are the eigenvectors of equation (2), correspond to the non-normalized photoelectron continuum orbitals, which are matched with regular and irregular Coulomb wave functions [16] in order to normalize them according to the **K**-matrix asymptotic conditions. Dipole matrix elements in the length gauge are then calculated between the initial core orbital and the final continuum, which are further transformed according to incoming waves **S**-matrix boundary conditions. Such dipole matrix elements are given as

$$D_{lh}^{\lambda\mu-}(\lambda_r) = \left\langle \varphi_{lh}^{\lambda\mu-} \middle| \Phi_{\lambda_r}^{\mathrm{EXT}} | \varphi_a \right\rangle, \tag{3}$$

where φ_a corresponds to the initial core orbital, $\Phi_{\lambda_r}^{\mathrm{EXT}}$ to each of the three components of the electric dipole operator which

transform like the standard spherical harmonics with $l = 1$ and $m = \lambda_r$, $\varphi_{lh}^{\lambda\mu-}$ is the continuum normalized according to the incoming wave boundary conditions. The continuum orbital is labeled by λ (the irreducible representation), μ (the subspecies in case of degeneracy), l (asymptotic angular momentum), and h is used to identify different elements with the same $\{l,\lambda,\mu\}$.

Following the treatment of photoionization for fixed molecular orientation given by Chandra [17], the angular distribution of the photoelectrons into the solid angle $d\hat{k}$ along their direction of propagation $\hat{k}$ from a molecule is expressed by

$$\frac{d^2\sigma}{d\Omega d\hat{k}} = (-1)^{m_r}\left(\frac{16\pi^3\alpha\omega n_i}{3}\right)\sum_L\sum_{M=-L}^{L} C_{LM}(k,\Omega)Y_{LM}(\hat{k}), \quad (4)$$

where Ω represents the Euler angles which define the molecular fixed orientation with respect to the laboratory (photon) frame, α is the fine structure constant, n_i is the occupation number of the ionized orbital, and m_r is 0, +1 or −1 for linear, left circular, or right circular polarization, respectively. The laboratory frame is defined by the incident photons; the polar axis corresponds to the electric vector or propagation direction for linear or circular light polarization, respectively.

Finally, the C_{LM} coefficients are obtained from the following expression [17,18]:

$$\begin{aligned} C_{LM}(k,\Omega) = & \sum_{\substack{\lambda,\mu,h,l,m,\lambda_r \\ \lambda',\mu',h',l',m',\lambda_r'}} (-i)^{l-l'} e^{i(\sigma_l-\sigma_{l'})}(-1)^{m+\lambda_r} \\ & \times \left[\frac{(2l+1)(2l'+1)(2L+1)}{4\pi}\right]^{1/2} \\ & \times \begin{pmatrix} l & l' & L \\ 0 & 0 & 0 \end{pmatrix}\begin{pmatrix} l & l' & L \\ -m & m' & M \end{pmatrix} b_{lmh}^{\lambda\mu} b_{l'm'h'}^{\lambda'\mu'*} \\ & \times D_{lh}^{\lambda\mu-}(\lambda_r) D_{l'h'}^{\lambda'\mu'-}(\lambda_r')^* \sum_{L_r}(2L_r+1) \\ & \times \begin{pmatrix} 1 & 1 & L_r \\ -m_r & m_r & 0 \end{pmatrix}\begin{pmatrix} 1 & 1 & L_r \\ -\lambda_r & \lambda_r' & \lambda_r-\lambda_r' \end{pmatrix} \\ & \times R^{L_r}_{\lambda_r-\lambda_r',0}(\Omega), \end{aligned} \quad (5)$$

where $R^{L_r}_{\lambda_r-\lambda_r',0}(\Omega)$ are the rotation matrices, σ_l are the Coulomb phase shifts, $b_{lmh}^{\lambda\mu}$ are the coefficients which adapt the spherical harmonics to the point group symmetry, and the Wigner $3j$ symbols are employed. The theoretical polar plots reported in this work are therefore calculated by expanding expression (4), with the coefficients $C_{LM}(k,\Omega)$ obtained from (5). Finally, we have also employed the complex dipoles of expression (3) as initial guesses to fit the experimental photoelectron angular distribution. More precisely, we split the complex dipole into its absolute value d and a short-range phase shift τ:

$$D_{lh}^{\lambda\mu-}(\lambda_r) = d_{lh}^{\lambda_r} e^{i\tau_{lh}} \quad (6)$$

In the present calculations, the LCAO B-spline basis set has been built as follows: a large expansion has been set on the center of mass of the molecule, with functions up to angular momentum 10, and with a radial grid extending up to 20 a.u. with step size 0.2 a.u. Smaller off-center B-spline expansions (LCAO) have been set over the C and H nuclei within a sphere of radius 0.8 a.u. with step size 0.2 a.u., the angular momentum up to 1 and 0 for C and H respectively.

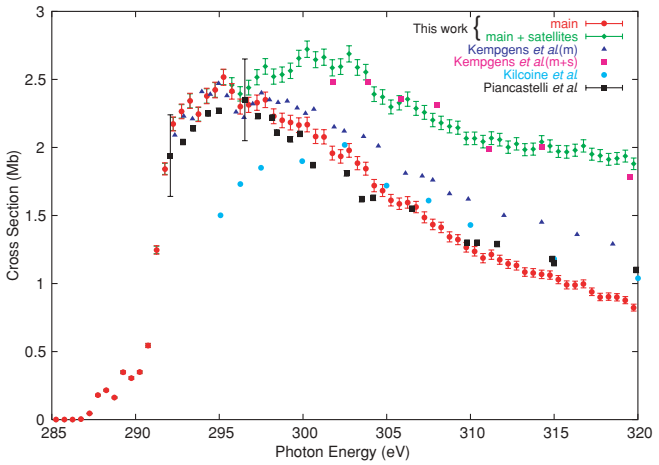

FIG. 5. (Color) Measured total cross section versus the photon energy. Results from this work are compared to the results from [12,27,28].

V. ANALYSIS RESULTS AND COMPARISON WITH THEORY

The data collection during the experiment was done in two types of runs. The first type was a photon-energy scan with a very fine step size (∼0.1 eV). The data, collected and properly normalized in this regime, were used to obtain the total reaction cross section. Figure 5 shows how it compares to previously measured results. In this work only, the relative, as opposed to absolute, cross sections were measured. The results displayed in Fig. 5 were scaled to match the peak of the distribution to the most resent measurements by Kempgens *et al.* in [12]. There is an excellent agrement of our results with the previous measurements, in particular with those presented by Kempgens *et al.* in [12].

The second type consisted of a series of much longer runs of 10 different photon-energy points across the predicted shape resonance position. The data collected here was used to produce the photoelectron angular distribution in a body-fixed frame for each of those energy points.

The 4π collection solid angle for all the reaction products means that the data represent comprehensive coverage of the entire multi-dimensional space spanned by the momentum space of the photoelectrons for every vector alignment of the molecular axis and all KERs of the fragmentation. To convert the results into the form of a finite number of relevant plots which can properly describe the reaction, one has to slice the experimental data in several different directions. Each of these slices offers a specific view at the multi-dimensional reaction cross section.

A. Total cross sections

An important parameter obtained from the photoelectron angular distribution is the ratio of the sigma and pi cross sections. By definition, the σ ($\hat{\varepsilon}$ parallel to molecular axis) and π ($\hat{\varepsilon}$ perpendicular to molecular axis) cross sections are

given by

$$\left.\frac{d\sigma}{d\Omega_\varepsilon}\right|_{\theta_\epsilon=0^\circ} = \sigma, \quad \left.\frac{d\sigma}{d\Omega_\varepsilon}\right|_{\theta_\epsilon=90^\circ} = \pi, \tag{7}$$

or, in the general case (as long as the initial state of the system is an even or odd function of φ):

$$\frac{d\sigma}{d\Omega_\varepsilon} = \sigma \cos^2(\theta_\varepsilon) + \pi \sin^2(\theta_\varepsilon), \tag{8}$$

where θ_ε is the polarization direction relative to the molecular frame.

According to (7), the first and the last frames of Fig. 4 can be integrated over the electron direction and the ratio of totals can be taken as σ/π while canceling out the arbitrary scaling factor. For a better result, we minimized the error bars due to the small solid angles by integrating all of the data that went into Fig. 4 (not just the first and last frame) over the electron direction. The resulting plot was fitted by the function form (8) and a more accurate ratio of σ/π was obtained. This procedure was repeated for all 10 different photon energies.

The integration of (8) over all polarization directions in turn readily yields the formula for the total cross section in terms of σ and π: total cross section $\propto \sigma + 2\pi$. Thus, the absolute cross section as a function of energy together with σ/π information can be used to get absolute values for the σ and π contributions:

$$\begin{cases} f(h\nu) = \sigma + 2\pi \\ g(h\nu) = \sigma/\pi \end{cases} \Rightarrow \begin{cases} \sigma = \frac{f(h\nu)g(h\nu)}{2+g(h\nu)}, \\ \pi = \frac{f(h\nu)}{2+g(h\nu)}. \end{cases}$$

The plot of the results is shown in Fig. 6. The theoretical calculations are shown as the solid curves in this figure and are in excellent agreement with the experimental results (scaled to fit). The σ cross section broad structure peeking around 300 eV strongly supports the presence of the shape resonance.

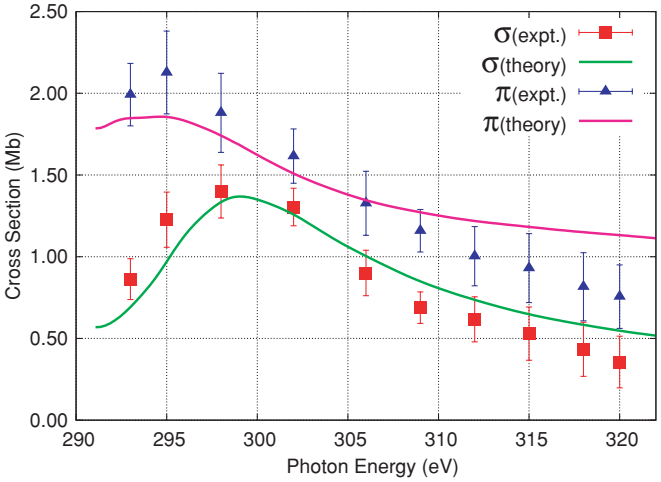

FIG. 6. (Color) Contributions of σ and π to the total cross section. Theoretical results shown with the smooth solid curves; error bars represent the experiment.

B. Differential cross sections

More impressive agreement of theory and experiment is observed when we compare the calculated and measured photoelectron angular distributions, examples of which are shown in Figs. 7, 8, and 9 for three different photon energies. Here the red solid curves represent the theoretical calculations rather than the spherical harmonic fits. Only a single scaling factor derived from the total cross-section values was used throughout all of the snapshots to compare the calculated curves to the experimental ones. It seems that the theoretical model works particularly well for the higher photon energies.

It is worth noting some specific aspects of the differential cross section plots, starting with the results at 293 eV (Fig. 7). At 0° (parallel polarization), the photoelectrons are preferably emitted along the C–C bond direction, with only minor emission in the perpendicular direction, which is, in any case, predicted by the theory and confirmed by the experiment. At 90° (perpendicular polarization), the photoelectrons are preferentially emitted along the diagonal directions, a typical behavior already observed in diatomic molecules [18]. Notice that the theory is able to capture all the relevant features of the angular distributions at every polarization angle between the two limiting cases just considered.

The next energy, 302 eV (Fig. 8), is interesting because it is the closest to the shape resonance. At parallel polarization, the emission along the C–C bond direction is accompanied by four weak but angularly very well-resolved lobes pointing at about 60°, 120°, 240°, and 300°. They are also present in both experiment and calculation, and are the most evident and clear manifestation of the *f*-wave nature ($l = 3$) of the shape resonance. The perpendicular polarization angular distribution essentially keeps the shape of the previous energy, and this is not surprising because the "*f*-shape" resonance is supported by the σ continuum channel, which is not active for perpendicular polarization. The results at intermediate polarization angles also show interesting differences with respect to the previous energy. Consider, for example, the angular distribution at 20°: while the lobes along the C–C bond directions are similar, the relative intensity of the weaker diagonal lobes show an inverted intensity distribution. This inversion of the small lobes is a direct consequence of the shape resonance. Across a resonance, the phase of the continuum wave function changes by π. Since the shape resonance is only in the sigma and not in the pi channel, the relative phase between the σ and π contributions changes. The strongest effect can be observed when the polarization direction is around 45° with respect to the molecule. The resulting cross section, being the superposition of the comparable σ and π contributions [$\sin(45^\circ) = \cos(45^\circ) = 1/\sqrt{2}$], strongly depends on the relative phase between the two. Consequently, the linear dichroism, denoted by the $\cos\delta$ term (see equation (2) in [19]), is exhibited. As the relative phase δ changes across the shape resonance the direction of the constructive interference in the photoelectron angular distribution flips from about −60° (Fig. 7, bottom-left frame) to 60° (Fig. 8, bottom-left frame).

Finally, let us consider the highest energy results at 318 eV (Fig. 9). In this case, we are again off resonance. The parallel polarization results show again very weak emission away from the C–C bond. On the other hand, the perpendicular

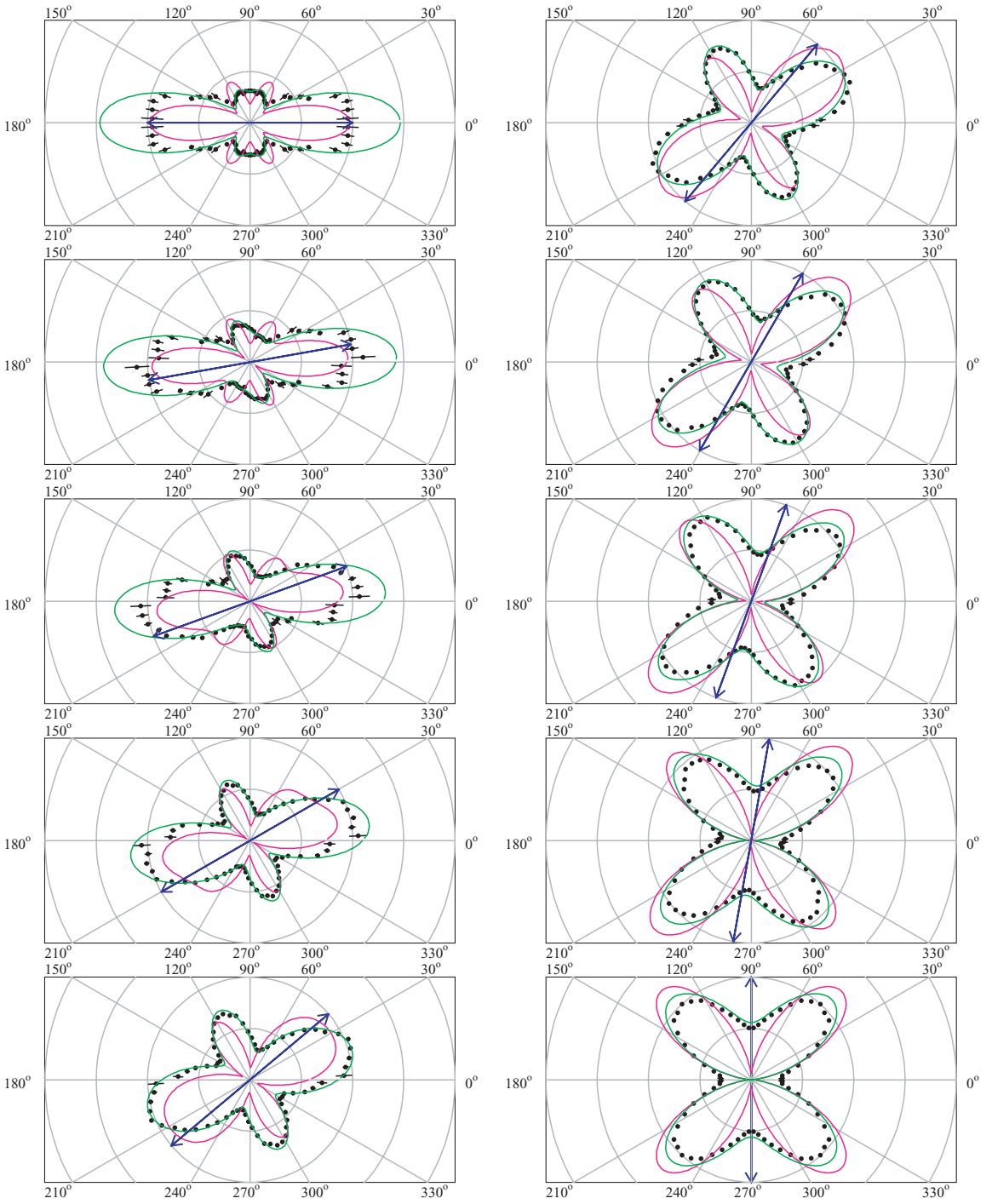

FIG. 7. (Color) Electron angular distribution at a photon energy of 293 eV. The arrow shows the direction of the polarization. Molecular orientation is always along the x axis. Red curves are theoretical angular distributions. Green curves are the results of a best fit.

polarization results show a much more structured pattern. This may be ascribed to a molecular geometry effect in which parallel polarization generates photoelectrons with σ symmetry that may strongly feel the C–C chemical bond, whereas perpendicular ionization generates photoelectrons with π symmetry which feel the C–C chemical bond to a lesser extent since they have a nodal line over it. However, as the energy increases, the photoelectron can penetrate better into the molecule and starts to feel the C–C chemical bond only at higher energy, showing more structure in an angular distribution pattern.

To further compare the results, an attempt was made to extract the set of dipole matrix transition elements (absolute values and relative phases), defined earlier in (6).

First recall the functional form (1) which was used to fit the experimental photoelectron angular distributions, as in Fig. 4. This fitting form was produced from a more general expression of the differential cross section that particularly emphasizes its

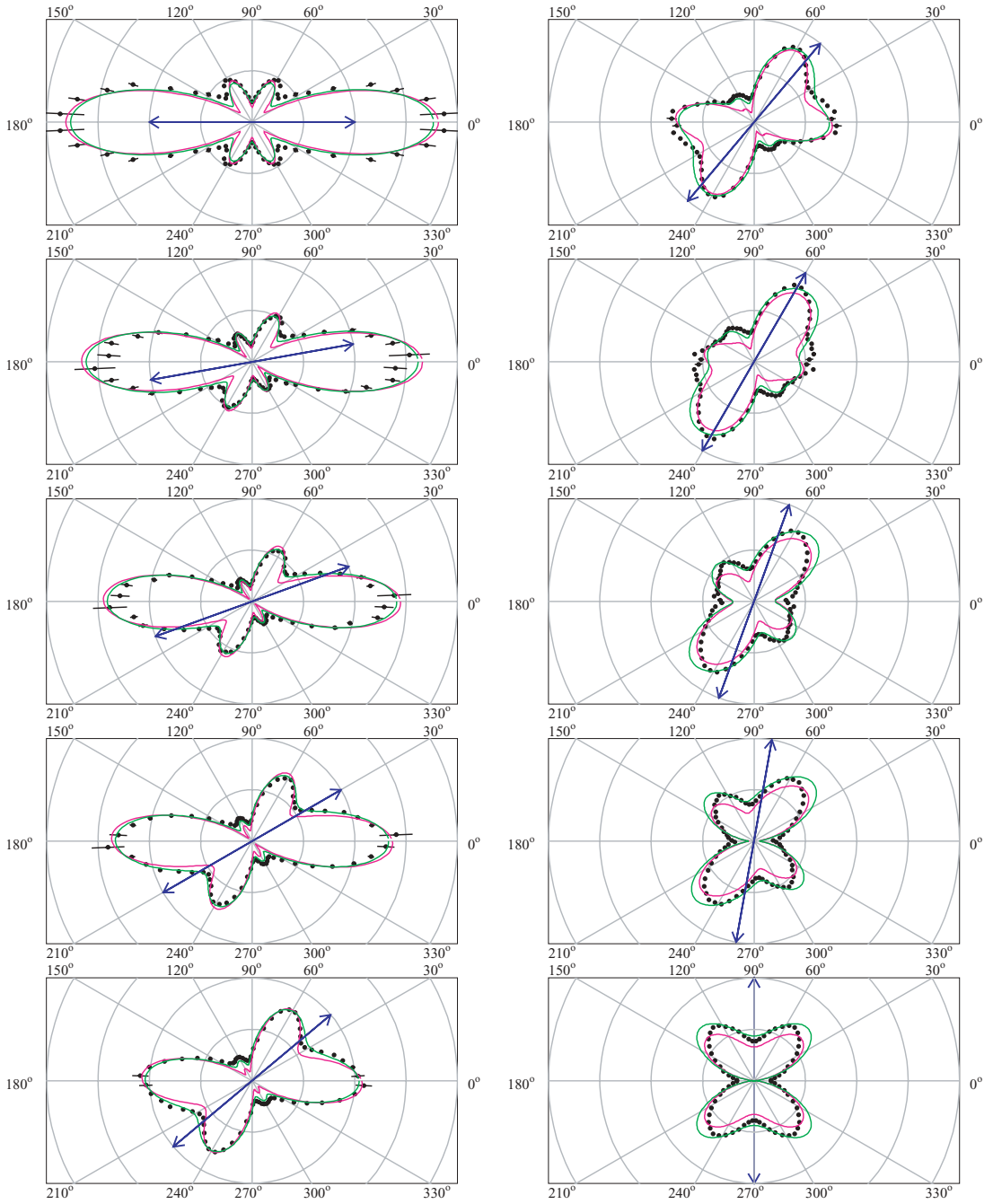

FIG. 8. (Color) Electron Angular Distribution at a photon energy of 302 eV. The arrow shows the direction of the polarization. Molecular orientation is always along the x axis. Red curves are theoretical angular distributions. Green curves are results of a best fit.

angular dependencies:

$$\frac{d^2\sigma}{d\mathbf{k}d\Omega} \propto \left|\sum_{l_{\text{odd}}} A_l(k)Y_l^0(\hat{\mathbf{k}})Y_1^0(\hat{\varepsilon}) + \sum_{l_{\text{odd}}} B_l(k)Y_l^{\pm1}(\hat{\mathbf{k}})Y_1^{\mp1}(\hat{\varepsilon})\right|^2 + \left|\sum_{l_{\text{even}}} A_l(k)Y_l^0(\hat{\mathbf{k}})Y_1^0(\hat{\varepsilon}) + \sum_{l_{\text{even}}} B_l(k)Y_l^{\pm1}(\hat{\mathbf{k}})Y_1^{\mp1}(\hat{\varepsilon})\right|^2,$$

where the two squared terms are due to the symmetry of the molecule and correspond to the gerade (g) and ungerade (u) initial states, which cannot be experimentally resolved so both contribute incoherently to the final cross section (alternatively, see [20–22] for a discussion of the possible coherence of the g and u contributions). The summations were truncated at $l = 3$. When the electric dipole operator acts on the states with cylindrical symmetry ($m = 0$) the only $Y_l^m(\hat{\mathbf{k}})$ that contribute to the final state are those with $m = 0, \pm1$, mimicking the m number of the photon. This is reflected in the above formula as well. In this case the A_l and B_l can be expressed through

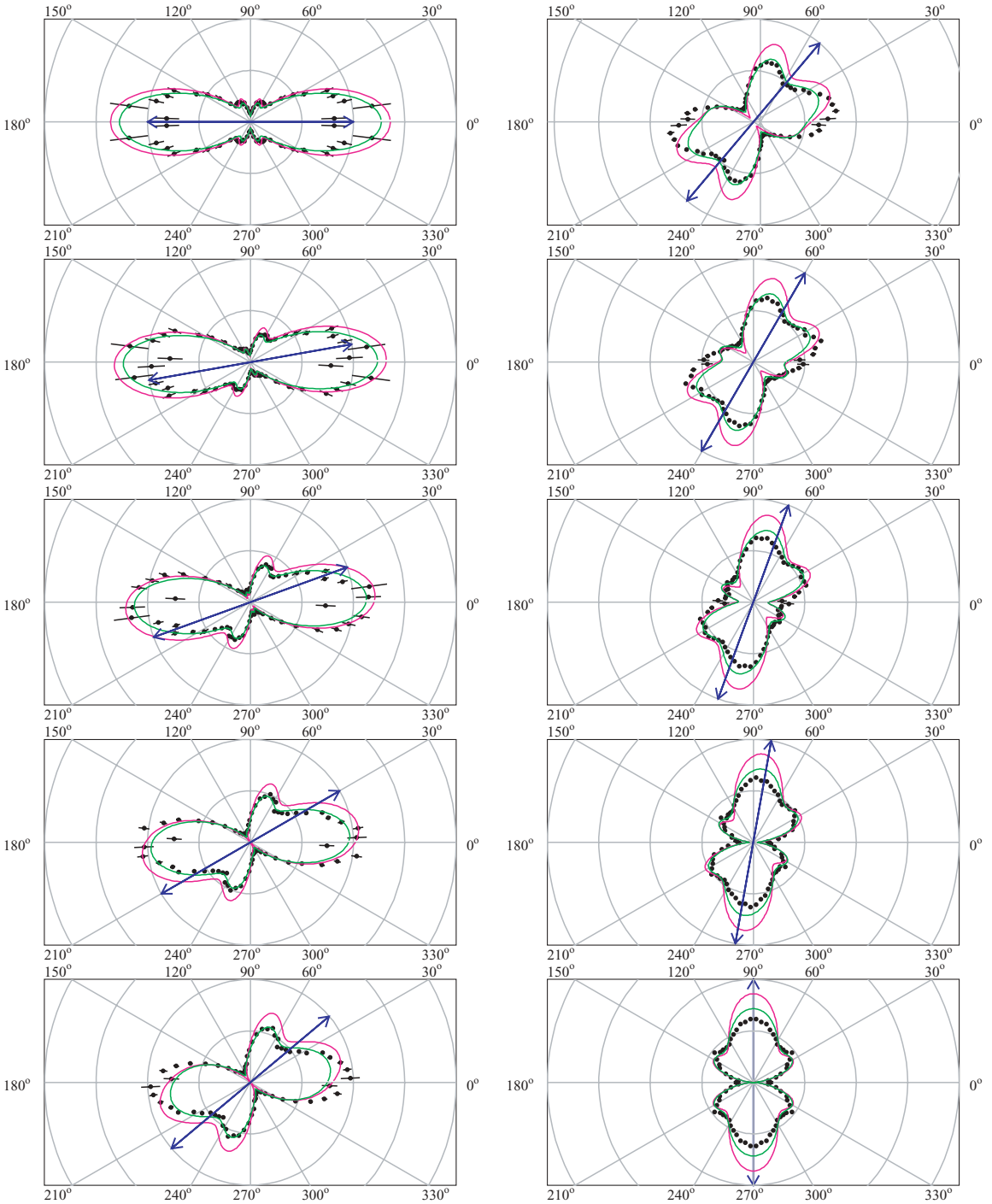

FIG. 9. (Color) Electron angular distribution at a photon energy o f318 eV. The arrow shows the direction of the polarization. Molecular orientation is always along the x axis. Red curves are theoretical angular distributions. Green curves are results of a best fit.

simplified set of complex dipoles, defined by (6), as

$$A_l \propto (-i)^l d_{l0} e^{(i\tau_{l0})}/\sqrt{p}, \quad B_l \propto (-i)^l d_{l1} e^{(i\tau_{l1})}/\sqrt{p}.$$

Strictly speaking, however, the above fitting functional form ($m = 0, \pm 1$) works only for linear molecules like O_2, N_2 (see [23]), or even C_2H_2. Another linear but not symmetric molecule that was a subject of a similar treatment in [24] is CO. On the other hand, C_2H_4 is a planar molecule, not linear, which was taken fully into account by the theoretical model. In fact, in the calculations of the time-dependent density functional theory (TDDFT) theoretical profiles all m contributions have been considered, up to $m = \pm 10$. To better match the theoretical treatment a more involved fitting procedure was performed with the extended functional form

given by

$$\left|\sum_{l_{\rm odd}}\sum_{m=-l}^{l}\sum_{m'=0,\pm1}\frac{(-i)^l d_{lm}^{m'}(k)\exp\left[i\tau_{lm}^{m'}(k)\right]}{\sqrt{p}}Y_l^m(\hat{\mathbf{k}})Y_1^{m'}(\hat{\varepsilon})\right|^2+\left|\sum_{l_{\rm even}}\sum_{m=-l}^{l}\sum_{m'=0,\pm1}\frac{(-i)^l d_{lm}^{m'}(k)\exp\left[i\tau_{lm}^{m'}(k)\right]}{\sqrt{p}}Y_l^m(\hat{\mathbf{k}})Y_1^{m'}(\hat{\varepsilon})\right|^2. \quad (9)$$

All m values here are due to the fact that initial state has no cylindrical symmetry and thus also has all possible m values (not just $m=0$).

Unfortunately, if form (9) is used to fit the experimental angular distributions with $d_{lm}^{m'}$ and $\tau_{lm}^{m'}$ as parameters, the procedure does not produce a unique set of best values for these parameters. The main reason is that the square of both odd and even functions is even, thus making the two terms in (9) not completely orthogonal or linearly independent. For this reason, the fitting was performed by assigning the $d_{lm}^{m'}$ and $\tau_{lm}^{m'}$ initial values to those produced by the theoretical calculations and letting them vary to get to the closest local minimum of χ^2. The photoelectron angular distributions resulting from this fitting procedure are shown as a green curve on top of the experimental results and theoretical angular distributions for three different photon energies in Figs. 7, 8, and 9. The values for the fitting parameters of the harmonics that contribute the most (these are harmonics that would contribute in the case of the linear molecule; i.e., $m=m'=0$ and $m=-m'=\pm1$) are plotted for all ten photon energies in Figs. 10, 11, 12, and 13. Since experiment cannot provide the absolute phase information, to obtain a better representation of actual phases and, more importantly, phase changes, the fitted results were obtained for the relative phases with respect to the first term of each (gerade and ungerade) contribution, and then the theoretically calculated phase of those terms were added to the experimental relative phases before plotting them:

$$\begin{aligned}\text{even } l &\Rightarrow \tau_{lm}=(\tau_{lm}-\tau_{00})_{\rm expt}+\tau_{00\rm theor},\\ \text{odd } l &\Rightarrow \tau_{lm}=(\tau_{lm}-\tau_{10})_{\rm expt}+\tau_{10\rm theor}.\end{aligned} \quad (10)$$

Good qualitative agreement between theory and experiment is clear. One particular feature that deserves special attention is the character of the sigma contribution of the $l=3$ partial wave. The amplitude clearly exhibits a peak at around 300 eV (green in Fig. 10) and its relative phase undergoes a change close to π in value (green in Fig. 11), which is consistent with the flipping of the minor lobes in the photoelectron angular distributions across the shape resonance, as just discussed. This is the most comprehensive confirmation of the presence of the f-wave shape resonance which was debated by several experimental and theoretical studies [12,25–28].

Slight quantitative disagreement of the results can be attributed to several factors besides the obvious deficiency of the fitting function form and the fitting software. The expansion in (9) was limited to $l\leqslant 7$ in the theoretical calculations, while in the fitting procedure only $l=0,\ldots,3$; $m=0,\pm1$ coefficients were varied, while the rest of the contributions were kept constant at the values given by the theory; finite acceptance angles used in experiments were not taken into account when fitting the angular distributions. As just mentioned, experimental photoelectron angular distributions were obtained with respect to the C–C bond, but random orientation of the molecular plane, while theory predicts only minor qualitative difference for different orientations, the complete angular distributions were obtained strictly in the plane of the molecule. Overall statistics and error bars of the experimental results could be improved, thus producing a more clear minimum in χ^2.

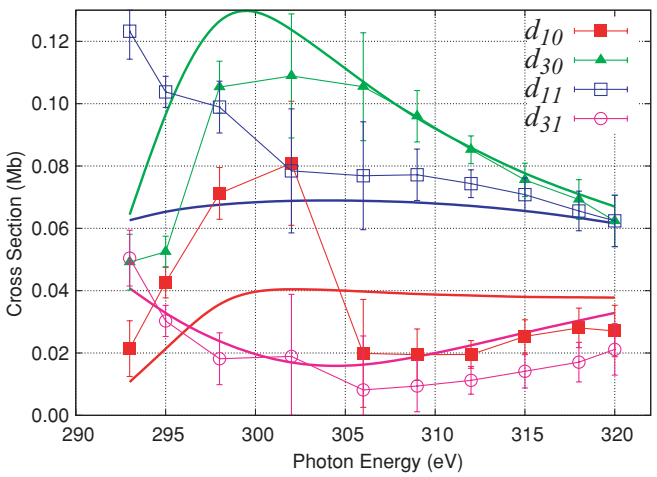

FIG. 10. (Color) Odd-l contribution amplitudes. Smooth curves are theoretical calculations for the respective parameters.

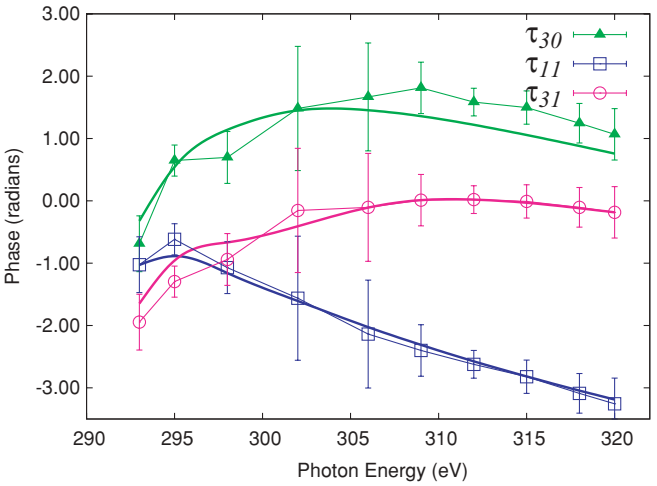

FIG. 11. (Color) Odd-l contribution phases. Smooth curves are theoretical calculations for the respective parameters.

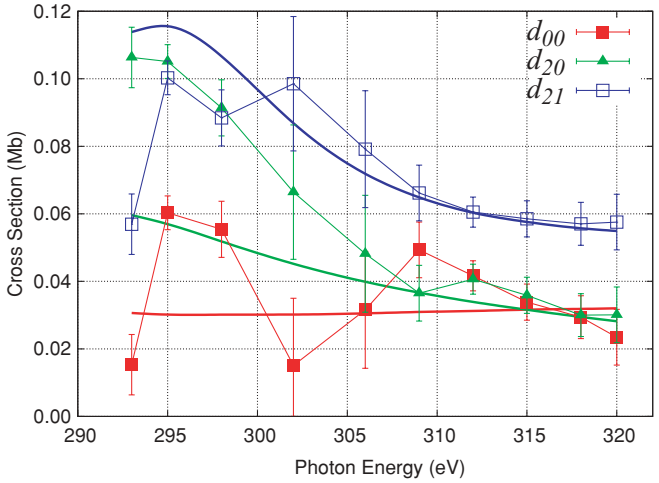

FIG. 12. (Color) Even-l contribution amplitudes. Smooth curves are theoretical calculations for the respective parameters.

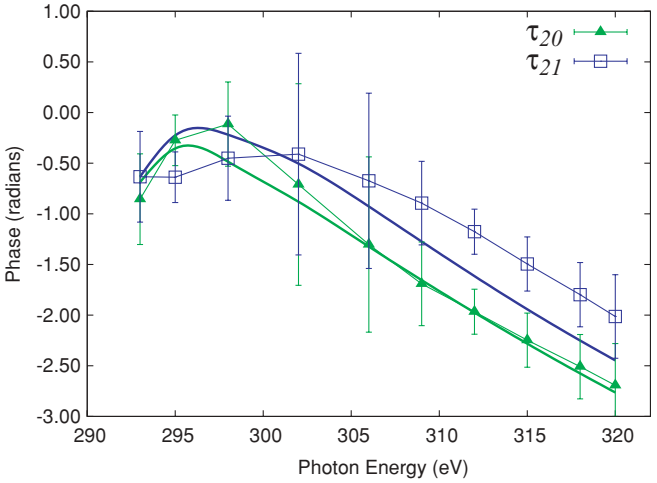

FIG. 13. (Color) Even-l contribution phases. Smooth curves are theoretical calculations for the respective parameters.

VI. CONCLUSIONS

Using the COLTRIMS technique, we performed a kinematically complete experiment measuring photoionization of the carbon K-edge of fixed-in-space C_2H_4. Coincidence measurements of reaction products along with data collection and analysis on an event-by-event basis allowed us to obtain the multi-differential angular distribution of photoelectrons (ADPs) in the body-fixed frame of the ethylene molecule. We also completed a very comprehensive theoretical study of the reaction. A set of dipole-transition matrix elements was calculated and extracted (7 amplitudes and 5 relative phases) from the experimental results. These matrix elements along with the complete ADPs showed a very good qualitative agreement between the experiment and the theoretical model used. The behavior of the $l = 3$, $m = 0$ partial wave contribution, obtained from both calculations and experiment, indisputably confirms the presence of the ethylene f-wave shape resonance found around 10 eV above the carbon K-edge.

In general, such a validation of the theoretical approach, as presented in this article, assures its successful utilization in studying and describing the parameters and features of the ethylene molecule; its geometrical structure, chemical activities, and physical properties, as well as predicting and even controlling chemical and atomic reactions other than just carbon K-edge photoionization studied in this work.

ACKNOWLEDGMENTS

The calculations have been supported by grants from MIUR (Programmi di Ricerca di Interesse Nazionale PRIN 2006) of Italy, from Consorzio Interuniversitario Nazionale per la Scienza e Tecnologia dei Materiali (INSTM) and from CINECA (Bologna, Italy). Experimental work has been supported by the US Department of Energy, Office of Science, Office of Basic Energy Sciences, Chemical Sciences, Geosciences, and Biosciences Division. Support from the DAAD and DFG is acknowledged.

[1] E. Shigemasa, J. Adachi, M. Oura, and A. Yagishita, Phys. Rev. Lett. **74**, 359 (1995).
[2] R. N. Zare, Mol. Photochem. **4**, 1 (1972).
[3] T. Osipov, C. L. Cocke, M. H. Prior, A. Landers, Th. Weber, O Jagutzki, L. Schmidt, H. Schmidt-Böcking, and R. Dörner, Phys. Rev. Lett. **90**, 233002 (2003).
[4] T. Weber, O. Jagutzki, M. Hattass, A. Staudte, A. Nauert, L. Schmidt, M. H. Prior, A. L. Landers, A. Bräuning-Demian, H. Bräuning, C. L. Cocke, T. Osipov, I. Ali, R. Diez Muñoz, D. Rolles, F. J. Garcia de Abajo, C. S. Fadley, M. A. Van Hove, A. Cassimi, H. Schmidt-Böcking, and R. Dörner, J. Phys. B **34**, 3669 (2001).
[5] J. Ullrich, R. Moshammer, A. Dorn, R. Dörner, L. P. H. Schmidt, and H. Schmidt-Böcking, Rep. Prog. Phys. **66**, 1463 (2003).
[6] R. Dörner, V. Mergel, O. Jagutzki, L. Spielberger, J. Ullrich, R. Moshammer, and H. Schmidt-Böcking, Phys. Rep. **330**, 95 (2000).
[7] T. Osipov, Ph.D. thesis, Kansas State University, 2003.
[8] O. Jagutzki, V. Mergel, K. Ullmann-Pfleger, L. Spielberger, U. Spillmann, R. Dörner, and H. Schmidt-Böcking, Nucl. Instrum. Methods Phys. Res. A **477**, 244 (2002).
[9] RoentDek (http://www.roentdek.com).
[10] W. Wiley and I. McLaren, Rev. Sci. Instrum. **26**, 1150 (1955).
[11] R. Moshammer, M. Unverzagt, W. Schmitt, J. Ullrich, and H. Schmidt-Böcking, Nucl. Instrum. Methods Phys. Res. B **108**, 425 (1996).
[12] B. Kempgens, H. M. Köppe, A. Kivimäki, M. Neeb, K. Maier, U. Hergenhahn, and A. M. Bradshaw, Phys. Rev. Lett. **79**, 35 (1997).

[13] D. Toffoli, M. Stener, G. Fronzoni, and P. Decleva, Chem. Phys. **276**, 25 (2002).
[14] E. J. Baerends, D. E. Ellis, and P. Ros, Chem. Phys. **2**, 41 (1973).
[15] R. van Leeuwen and E. J. Baerends, Phys. Rev. A **49**, 2421 (1994).
[16] A. R. Barnett, Comput. Phys. Commun. **27**, 147 (1982).
[17] N. Chandra, J. Phys. B **20**, 3405 (1987).
[18] M. Stener, Chem. Phys. Lett. **356**, 153 (2002).
[19] T. Jahnke, T. Weber, A. L. Landers, A. Knapp, S. Schössler, J. Nickles, S. Kammer, O. Jagutzki, L. Schmidt, A. Czasch, T. Osipov, E. Arenholz, A. Young, R. Diez Muñoz, D. Rolles, F. J. Garcia de Abajo, C. S. Fadley, M. A. Van Hove, S. K. Semenov, N. A. Cherepkov, J. Rösch, M. H. Prior, H. Schmidt-Böcking, C. L. Cocke, and R. Dörner, Phys. Rev. Lett. **88**, 073002 (2002).
[20] M. S. Schöffler, J. Titze, N. Petridis, T. Jahnke, K. Cole, L. P. H. Schmidt, A. Czasch, D. Akoury, O. Jagutzki, J. B. Williams, N. A. Cherepkov, S. K. Semenov, C. W. McCurdy, T. N. Rescigno, C. L. Cocke, T. Osipov, S. Lee, M. H. Prior, A. Belkacem, A. L. Landers, H. Schmidt-Böcking, T. Weber, and R. Dörner, Science **320**, 920 (2008).
[21] N. A. Cherepkov, S. K. Semenov, M. S. Schöffler, J. Titze, N. Petridis, T. Jahnke, K. Cole, L. P. H. Schmidt, A. Czasch, D. Akoury, O. Jagutzki, J. B. Williams, C. L. Cocke, T. Osipov, S. Lee, M. H. Prior, A. Belkacem, A. L. Landers, H. Schmidt-Böcking, Th. Weber, and R. Dörner, Phys. Rev. A **80**, 051404(R) (2009).
[22] N. A. Cherepkov, S. K. Semenov, and R. Dörner, J. Phys. Conf. Series **141**, 012001 (2008).
[23] S. Motoki, J. Adachi, K. Ito, K. Ishii, K. Soejima, A. Yagishita, S. K. Semenov, and N. A. Cherepkov, J. Phys. B **35**, 3801 (2002).
[24] N. A. Cherepkov, G. Raseev, J. Adachi, Y. Hikosaka, K. I. S. Motoki, M. Sano, K. Soejima, and A. Yagishita, J. Phys. B **33**, 4213 (2000).
[25] N. Haack, G. Ceballos, H. Wende, K. Baberschke, D. Arvanitis, A. L. Ankudinov, and J. J. Rehr, Phys. Rev. Lett. **84**, 614 (2000).
[26] J. Berkowitz, *Photoabsorption, Photoionisation and Photoelectron Spectroscopy* (Academic, New York, 1979).
[27] M. N. Piancastelli, T. A. Ferrett, D. W. Lindle, L. J. Medhurst, P. A. Heimann, S. H. Liu, and D. A. Shirley, J. Chem. Phys. **90**, 3004 (1989).
[28] A. L. D. Kilcoyne, M. Schmidbauer, A. Koch, K. J. Randall, and J. Feldhaus, J. Chem. Phys. **98**, 6735 (1993).